Astronomy & Astrophysics manuscript no. output
October 1, 2025

Impact of nonthermal electron distributions on the triggering of the ion-ion acoustic instability near the Sun: Kinetic simulations

Mahmoud Saad Afify[1, 2], Jürgen Dreher[1], Stuart O'Neill[1], and Maria Elena Innocenti[1]

[1] Theoretische Physik I, Ruhr-Universität Bochum, Bochum, Germany
[2] Department of Physics, Faculty of Science, Benha University, Benha 13518, Egypt
e-mail: `Mahmoud.Ibrahim@ruhr-uni-bochum.de`
`Mahmoud.Afify@fsc.bu.edu.eg`

Received August 18, 2025

ABSTRACT

Context. We previously investigated the stability threshold of the ion-ion acoustic instability (IIAI) in parameter regimes compatible with recent Parker Solar Probe (PSP) observations, in the presence of a Maxwellian electron distribution. We find that the observed parameters are close to the instability threshold, but IIAI requires a higher electron temperature than what is observed.
Aims. As electron distributions in the solar wind present clear non-Maxwellian features, we investigated if deviations from the Maxwellian distribution could explain the observed IIAI. We address specifically the kappa (κ) and core-strahl distributions for the electrons.
Methods. We performed analytical studies and kinetic simulations using a Vlasov-Poisson code in a parameter regime relevant to PSP observations. The simulated growth rates were validated against kinetic theory.
Results. We show that the IIAI threshold changes in the presence of κ or core-strahl electron distributions, but not significantly. In the latter case, simulations confirm the expression of an effective temperature for an equivalent Maxwellian electron distribution. Such an effective temperature could simplify stability assessments of future observations.

Key words. Kappa-distribution - Strahl electrons - Solar wind - Electrostatic instabilities - Ion acoustic

Use \titlerunning to supply a shorter title and/or \authorrunning to supply a shorter list of authors.

1. Introduction

Observations of plasma in the solar wind and planetary magnetospheres over past decades have made it clear that non-Maxwellian distribution functions are ubiquitous (Feldman et al. 1973, 1974b, 1975; Maksimovic et al. 1997b; Marsch et al. 1982; Marsch & Livi 1987; Neugebauer et al. 1996; Marsch 2006, 2018; Klein et al. 2018; Ďurovcová et al. 2019). These non-thermal structures actively shape the large-scale dynamics of the solar wind by driving micro-instabilities (Štverák et al. 2009; Matteini et al. 2013), which in turn constrain large-scale solar wind parameters, influencing wave spectra (Verscharen & Marsch 2011; Yoon et al. 2024) and mediating particle transport (Marsch 2006; Reames 2021).

In situ measurements reveal that proton velocity distribution functions (VDFs) frequently deviate from Maxwellian equilibrium distributions in the solar wind. A common non-equilibrium feature is the presence of a field-aligned beam, which is a secondary proton population streaming faster than the core proton component along the magnetic field direction (Feldman et al. 1974b; Marsch et al. 1982; Alterman et al. 2018; Verniero et al. 2020, 2022). Moreover, proton VDFs often exhibit temperature anisotropies with respect to the local magnetic field (Marsch et al. 1981, 2004; Hellinger et al. 2006; Bale et al. 2009; Maruca et al. 2012). All these features are generally more pronounced in fast solar wind compared to slow wind (Verscharen et al. 2019). The presence of an ion beam, possibly anisotropic, plays a crucial role in driving a variety of ion-scale instabilities (Gary 1993; Gary et al. 1984, 1985; Daughton & Gary 1998; Verscharen et al. 2013; Verscharen & Chandran 2013; Gary et al. 2016). Extensive investigations of ion beam instabilities have been conducted using both hybrid simulations (Daughton et al. 1999; Gary et al. 2000; Wang & Lin 2003; Lu et al. 2006; Ofman et al. 2022, 2023, 2025) and fully kinetic particle-in-cell (PIC) approaches (Riquelme et al. 2015; Che et al. 2023; Pezzini et al. 2024). However, these studies have primarily focused on ion kinetic physics, often neglecting the effects of the non-Maxwellian electron VDFs commonly observed in the solar wind. Works that have examined the effect of non-Maxwellian electron VDFs on ion-scale instabilities have usually focused on anisotropic Maxwellian electron distributions (Ahmadi et al. 2016; Micera et al. 2020a; Walters et al. 2024).

Solar wind electron velocity distributions also exhibit distinct non-thermal characteristics. They typically comprise a thermal core component and a field-aligned, anti-Sunward propagating beam, the strahl (Feldman et al. 1973, 1974a, 1975; Pilipp et al. 1987; Lin 1998; Maksimovic et al. 2005; Štverák et al. 2009; Micera et al. 2020b, 2021, 2025). The core population, representing approximately 95 % of the total electron density, dominates the distribution. The strahl is composed of high-energy electrons that escaped solar gravity along open magnetic field lines and became focused about the field direction via the conservation of the first adiabatic invariant in a magnetic field of decreasing magnitude (Meyer-Vernet 2007). The halo - a third, thin, hot and often κ-distributed population - originates from scattering of the strahl population due to instabilities in the whistler family. This is demonstrated by the anti-correlation

Article published by EDP Sciences, to be cited as https://doi.org/10.1051/0004-6361/202556866

between halo and strahl densities (Maksimovic et al. 2005), direct in situ Parker Solar Probe (PSP) observations (Cattell et al. 2021), and particle-in-cell simulations (Micera et al. 2020b, 2021).

The κ-distributions are a type of non-thermal distribution characterised by a Maxwellian-like core and power-law tails that indicate an excess of high-velocity particles (Summers & Thorne 1991; Vasyliunas 1968; Maksimovic et al. 1997a). The suprathermal characteristics of the distribution increase as the parameter κ decreases, with the distribution becoming non-physical at the critical value $\kappa = 3/2$, where the mean kinetic energy becomes infinite, i.e. the super-thermal distribution becomes non-normalisable in terms of finite energy (Pierrard & Lazar 2010). At $\kappa = \infty$, a Maxwellian distribution is recovered. The distribution has been extensively used in kinetic models of the solar wind due to its convenience in modelling both the core and super-thermal populations, as well as the advantage of recovering a Maxwellian distribution at the high κ limit (Maksimovic et al. 1997b).

The PSP has provided invaluable insights into ion-scale instabilities in the solar wind. In fact, PSP observations have shown the ubiquity of ion-scale wave activity, including a number of 'ion storms' related to the presence of ion beams and anisotropies (Verniero et al. 2020, 2022). While most ion instabilities are electromagnetic in nature, the electrostatic ion-ion acoustic instability (IIAI) has been observed and characterised over a range of heliocentric distances (Mozer et al. 2020, 2021, 2023, 2025). The IIAI is driven by a proton core and beam drifting with respect to each other in the presence of high-temperature electrons, which minimises Landau damping (Gary & Omidi 1987; Silin & Uryupin 1992; Afify et al. 2024). We investigated IIAI onset in parameter regimes comparable with the observations in Mozer et al. (2021) and our previous work, Afify et al. (2024). We demonstrated through combined theoretical and simulation analysis that the solar wind parameters reported in Mozer et al. (2021) are in the vicinity of the IIAI threshold, but not yet in the unstable regime. In particular, we succeeded in reproducing the frequency, wavenumber, and magnitude of the high-frequency IIAI observed there, but only after slightly modifying key parameters such as the electron-to-proton-core temperature ratio, the ratio between the parallel-beam and the proton-core temperatures, and the relative drift between the core and beam protons. All our investigations were conducted in the presence of a Maxwellian electron population, which, as already mentioned, does not reflect the observed electron distribution in the solar wind.

Our aim now is to investigate if non-Maxwellian electron VDFs can promote the onset of the IIAI in parameter regimes compatible with those observed in Mozer et al. (2021). We started from one of the cases analysed in Afify et al. (2024), where the temperature ratio between the electron (e) and proton core (c) population increased from the observed $T_e/T_c \sim 7$ to $T_e/T_c = 10$. Similarly, the temperature ratio between the proton beam (b) and core component decreased from the observed $T_b/T_c = 2.7$ to $T_b/T_c = 1$. We considered two types of electron distributions. In Sec. 2 we start with κ-distributed electrons, often used to approximate the observed core plus supra-thermal electron distribution. We examine the effect of the κ parameter on the instability threshold. We then move to a core-strahl distribution, also Maxwellian, in Sec. 3. We investigate the IIAI threshold variation as a function of the electron strahl's density and temperature, and of the relative drift speed between the proton core and beam. Discussion and conclusions are presented in Sec. 4.

2. Kappa-distributed electrons

We first examined the impact of κ-distributed - as opposed to Maxwellian-distributed - electrons on the IIAI. We chose the 1D standard κ distribution given by Vasyliunas (1968), Summers & Thorne (1991), and Abdul & Mace (2014):

$$f(v) = \left(\pi\kappa\theta^2\right)^{-1/2} \frac{\Gamma(\kappa)}{\Gamma(\kappa - 1/2)} \left(1 + \frac{v^2}{\kappa\theta^2}\right)^{-\kappa}, \tag{1}$$

where $\theta^2 = 2[(\kappa - 3/2)/\kappa]v_{th,e}^2$ is the generalised thermal velocity, which is a function of the κ index. Here, $v_{th,e} = \sqrt{\frac{T_e}{m_e}}$ is the electron thermal velocity, with T_e (expressed in energy units) representing the average kinetic energy per particle. Figure 1 shows the velocity distributions of electrons and protons in our model of the non-thermal solar wind plasma. The left panel displays κ-distributed electrons for three different spectral indices, $\kappa = 20$, $\kappa = 7$, and $\kappa = 5$, with electron to proton core temperature $T_e/T_c = 10$. As κ decreases, the distribution develops a more pronounced high-energy tail, characteristic of supra-thermal populations. At the same time, the peak electron density at $v_e/v_{th,c} \sim 0$ increases (see inset). The right panel shows the combined distribution of protons, consisting of a Maxwellian-distributed core and a beam component, as an example case. Motivated by PSP observations reported in Mozer et al. (2021), we chose a proton beam-core drift speed of $V_d = 5\ v_{th,c}$, with $v_{th,c}$ the thermal speed of the proton core, equal beam and core temperatures ($T_b = T_c$), and a dilute proton beam ($n_b/n_c = 0.05$), with n_j the density of the population j and b the proton beam. These parameters are in the range of PSP observations close to the Sun (Mozer et al. 2021). We first calculated the dispersion relation of the IIAI, given by Eq. (3) from Afify et al. (2024), but now with κ-distributed electrons. The plasma dispersion function (Fried & Conte 1961) was evaluated numerically using the Faddeeva function as implemented in SciPy to find its roots (Virtanen et al. 2020). Figure 2a shows the dispersion relation for $\kappa = 20, 7$, and 5 in black, blue, and red, respectively. γ is the growth rate, normalised to the core proton plasma frequency, ω_{pc}. The wavenumber, k, is normalised to the core proton Debye length, λ_{Dc}. The parameters ($V_d/v_{th,c}$, n_b/n_c, T_e/T_c, and T_b/T_c) are the same as mentioned above. We described in Afify et al. (2024) how the maximum IIAI growth rate first increases and then decreases with increasing drift velocity in the case of Maxwellian electron distribution. This feature is also found with κ-distributed electrons, as shown in Fig. 2b. We see from both panels of Fig. 2 that for κ-distributed electrons, smaller κ values reduce the rate of instability growth.

We verified theoretical predictions with 1D1V Vlasov simulations, using the code described in Afify et al. (2024). The box length was $L_x/\lambda_{Dc} = 50$, with grid spacing $\Delta x/\lambda_{Dc} = 0.25$. The velocity spaces of protons (core and beam) and electrons were resolved with 151 and 193 points, respectively, with the electron grid extending up to 12 times its thermal speed. Boundary conditions were periodic along x and there was zero flux at $v = v_{min}, v_{max}$. We used the maximum value of the electric field in the simulation box as a measure for instability growth. The same parameters as Fig. 2a were used for the simulation run depicted in Fig. 3. The black lines superimposed on the linear phase of the instability mark the time interval used for growth rate calculations. A comparison between theoretical (Th) and simulated (Sim) growth rates at the simulated wavenumber $k\lambda_{Dc} = 2\pi/50 = 0.126$ is shown in Table 1, together with the real frequency of the instability and the resonance velocity given by

Landau theory (Th). The chosen simulated wavenumber is close to the maxima of the growth rate (see Fig. 2a).

Figure 4 presents simulation results illustrating how κ-distributed electrons modify the instability. These snapshots were taken at $\omega_{pc}t = 300$, when all simulations were approaching the end of the linear phase. The left columns depict the beam phase-space distribution function. We see traces of resonant beam interaction (ion hole formation), which are more developed at higher κ values, where the instability has reached a larger amplitude. In the middle and right columns we depict the beam and core VDFs, averaged in space, at $x/\lambda_{Dc} = 0$ and at $x/\lambda_{Dc} = 25$, respectively. The vertical dashed line indicates the resonance velocity, $v_{res} = \omega/k$, as calculated from linear theory at $k\lambda_{Dc} = 0.126$. The averaged velocity distribution, as well as the velocity distribution cuts at $x/\lambda_{Dc} = 0,\ 25$, shows that the velocity distribution is indeed modified in the vicinity of the resonant velocity. As the core protons were only very weakly affected by this resonant process, we plotted their velocity distribution on a logarithmic scale. Figure 5 shows time $\omega_{pc}t = 1000$, when the instability in all simulations has already saturated. We observed the effect of resonance interaction on the proton beam population. We observed that at lower κ values, signatures on both the proton core and beam population were weaker, consistent with smaller saturation amplitudes (see Fig. 3).

3. Core-strahl electrons

We then considered an alternative distribution for the electron population, namely the core-strahl distribution often observed in the solar wind. We used as the temperature for the electron core (ec) population $T_{ec} = 7\ T_c$, as in Mozer et al. (2021). With only one Maxwellian electron population at this temperature, the configuration was stable to the IIAI. We then redistributed part of these electrons into a hotter, Maxwellian strahl population and examined the resulting effects on the IIAI. We now had four populations: two proton (p) and two electron (e) populations, each composed of a core (c) and a beam. We labelled the proton beam b, in accordance with the nomenclature common in solar wind physics, but labelled the electron beam s instead of the usual 'strahl'. In this notation, the densities were related by $n_{ec} + n_{es} = n_b + n_c$. We varied the density and temperature of the strahl population and investigated the effects on the instability. Electron and proton cores were at rest in all these experiments. The density of the proton beam was kept fixed to the values analysed in the previous section, $n_b/n_c = 0.05$. The proton beam drift was kept at $V_d/v_{th,c} = 5$ unless specified otherwise. The drift velocity of the strahl resulted from the zero current condition, $V_{d,es} = V_d n_{pb}/n_{es}$.

Figure 6 shows that a hotter strahl component tends to destabilise the instability, as shown by the maximum normalised growth rate, $\gamma_{\max}/\omega_{pc}$, calculated from Landau theory and presented as a colour-coded contour plot. The left panel illustrates the dependence of the growth rate on two key parameters: the electron strahl-to-core proton temperature ratio (T_{es}/T_c) and the electron strahl-to-core proton density ratio (n_{es}/n_c). A denser, hotter strahl favours instability onset. In the right panel we changed only the strahl density, while keeping $T_{es}/T_c = 25$. In the vertical axis, we allowed the proton beam drift velocity, $V_d/v_{th,c}$, to change. The instability only exists in a finite V_d interval, which widens with increasing strahl density (see Afify et al. (2024) and Fig. 2b).

In Table 2 we list a number of cases where we changed the strahl temperature with a fixed strahl density $n_{es}/n_c = 0.2$ (cases A-D), and one (Case C') when we reduced the strahl density with respect to case C. As before, we provide real frequency and growth rates calculated at $k\lambda_{Dc} = 0.08$, from linear theory, and the growth rate obtained from simulations with box size $L_x/\lambda_{Dc} = 80$. Similarly, the chosen simulated wavenumber corresponded to the maximum growth rates as inferred from linear theory. In Fig. 7 we provide the full dispersion relation from theory (panel a) and the time history of the maximum electric field values from simulations (panel b) for the cases in Table 2.

There is a good agreement between the calculated and simulated growth rates, with a tendency for faster growth in simulations with respect to theory. Jones et al. (1975) calculated an effective electron temperature, T_{eff}, for IIAI evolution for an electron distribution composed of core and strahl:

$$T_{eff} = (n_e T_{es} T_{ec})/(n_{es} T_{ec} + n_{ec} T_{es}). \tag{2}$$

We calculated T_{eff} for our reference cases in Table 2. We used the same dispersion relation calculations and simulations to create Table 3 and Fig. 8 as we did for Table 2 and Fig. 7, using as the electron distribution a single Maxwellian with the temperature T_{eff} calculated from the corresponding core-strahl cases. We verified that theoretical results were identical and simulated results were fairly close, thus validating the concept of effective temperature. This is underpinned by the comparison of proton beam and core distributions in Fig. 9 (core-strahl electron distribution) and Fig. 10 (Maxwellian electron distribution, with $T_e = T_{eff}$). We observe the same wave-particle interaction patterns in both cases.

4. Discussion and conclusions

This study examines the influence of non-thermal electron populations, κ, and core-strahl on the triggering and evolution of the IIAI. It was motivated by previous results (Afify et al. 2024), where we found that a purely Maxwellian electron distribution would need slightly higher temperatures than those observed in Mozer et al. (2021) to allow for the observed IIAI-related wave activity.

The electron VDFs that we considered here are κ and core-strahl, which are customarily used to model observed electron VDFs in the solar wind. We find that κ-distributed electrons tend to stabilise the IIAI, with lower growth rates at lower κ indices. Adding a strahl distribution destabilises the IIAI with respect to a Maxwellian distribution. Stronger instabilities are observed for hotter and denser strahl populations.

Addressing the relationship with observations, we note that the strahl temperature of $T_{es}/T_c \approx 15-20$ used in our study corresponds to T_{es} being two to three times the electron core temperature and thereby might be fairly realistic for the solar wind. However, our $n_{es}/n_c = 0.15-0.2$ assumes a much denser strahl than the values of $0.05-0.1$ reported by Maksimovic et al. (2005) for solar distances of $0.3-1$ AU. Therefore, this study does not explain why IIAI-related wave activity is observed in Mozer et al. (2021). On the other hand, Maksimovic et al. (2005) also reported the strahl density to decrease with increasing solar distance, so a more massive electron strahl at PSP positions around 20 $R_\odot$ might be possible.

We obtained the following physical insights from this work: lower κ values tend to stabilise the IIAI due to the higher electron phase-space density at $v \sim v_{res} << v_{th,ec}$ (see inset of Fig. 1a), leading to enhanced Landau damping in the electrons. Since our parameters are very close to the instability threshold, even a slightly enhanced electron damping can determine the onset of instability. In the case of the core-strahl distribution, redistributing core electrons into a hotter strahl population reduces Landau damping and slightly increases the growth rate. This effect is captured in the formulation for an effective temperature provided by Jones et al. (1975) and is validated here with simulations. Using this concept, and assuming the limit of infinitively hot strahl electrons with a realistic strahl density $n_{es} = 0.05n_e$, the effective electron temperature would increase by only a few percent with respect to the electron core temperature; see Eq. 2 and the discussion in Jones et al. (1975). We speculate that the IIAI activity observed in Mozer et al. (2021) may be related to external drivers not captured in our model, for example temporary beam density or drift enhancements due to reconnection events, in conjunction with an increasing electron-to-proton temperature ratio, rather than to the specifics of the electron velocity distribution.

Acknowledgements. M. S. Afify thanks the Alexander von Humboldt Foundation, 53173 Bonn, Germany (Ref 3.4-1229224-EGY-HFST-P) for the research fellowship and its financial support. M.E.I. acknowledges support from the Deutsche Forschungsgemeinschaft (DFG, German Research Foundation) within the Collaborative Research Center SFB1491 and project 497938371. We thank J. Verniero and J. Halekas for useful discussion regarding PSP observations.

Table 1: Theoretical vs simulated instability parameters for κ-distributed electrons.

Name	κ	$(\omega/\omega_{pc})_{Th}$	$(v_{res}/v_{th,c})_{Th}$	$(\gamma/\omega_{pc})_{Th}$	$(\gamma/\omega_{pc})_{Sim}$
Case 1	20	0.434	3.442	0.0148	0.0161
Case 2	7	0.427	3.389	0.0101	0.0101
Case 3	5	0.422	3.352	0.0068	0.0053

Notes. The table compares theoretical (Th) growth rates, frequencies, and resonant velocities $v_{res} = \omega/k$ and observed simulation growth rates (Sim) for κ-distributed electrons with $T_e/T_c = 10$ and proton beams with $V_d/v_{th,c} = 5$, $n_b/n_c = 0.05$, and $T_b/T_c = 1.0$. Calculations were performed at a wavenumber of $k\lambda_{Dc} = 0.126$.

Table 2: Theoretical vs simulated instability parameters for core–strahl-distributed electrons.

Name	$\frac{n_{es}}{n_c}$	$\frac{T_{es}}{T_c}$	$(\omega/\omega_{pc})_{Th}$	$(v_{res}/v_{th,c})_{Th}$	$(\gamma/\omega_{pc})_{Th}$	$(\gamma/\omega_{pc})_{Sim}$
Case A	0.2	15.0	0.268	3.347	0.0039	0.00576
Case B	0.2	20.0	0.270	3.367	0.0049	0.00668
Case C	0.2	25.0	0.270	3.379	0.0055	0.00737
Case D	0.2	30.0	0.271	3.387	0.0059	0.00783
Case C'	0.15	25.0	0.268	3.349	0.0039	0.00587

Notes. The table compares theoretical (Th) growth rates, frequencies, and resonant velocities $v_{res} = \omega/k$ and observed simulation growth rates (Sim) for core–strahl-distributed electrons across various strahl densities and temperatures. Parameters kept fixed for all cases are $V_d/v_{th,c} = 5$, $n_b/n_c = 0.05$, $T_b/T_c = 1.0$, and $k\lambda_{Dc} = 0.08$.

Table 3: Same as Table 2 but using a single Maxwellian electron distribution with $T_e = T_{eff}$ instead of a core-strahl distribution.

Name	$\frac{T_{eff}}{T_c}$	$(\omega/\omega_{pc})_{Th}$	$(v_{res}/v_{th,c})_{Th}$	$(\gamma/\omega_{pc})_{Th}$	$(\gamma/\omega_{pc})_{Sim}$
Case A	7.792	0.268	3.347	0.004	0.00583
Case B	7.989	0.269	3.367	0.0051	0.00679
Case C	8.113	0.270	3.379	0.0057	0.00748
Case D	8.197	0.271	3.387	0.0061	0.00794
Case C'	7.803	0.268	3.349	0.0041	0.00592

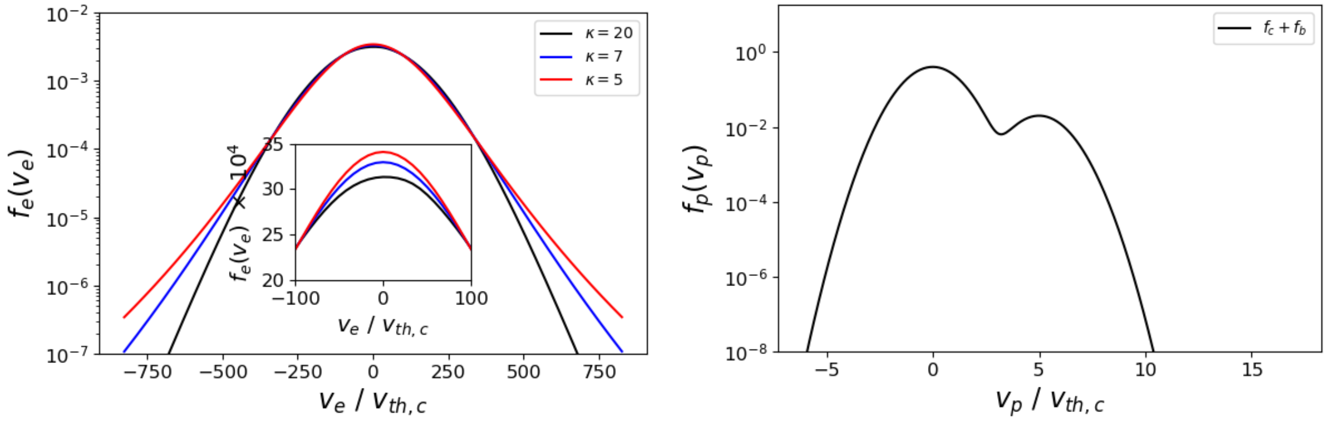

Fig. 1: Electron and proton distribution functions. Left: κ electron distributions with $T_e/T_c = 10$, $\kappa = 20$ (black curve), $\kappa = 7$ (blue curve), and $\kappa = 5$ (red curve). Right panel: Total proton distribution consisting of two Maxwellians (core and beam), with $V_d/v_{th,c} = 5$, $T_b/T_c = 1.0$, and $n_b/n_c = 0.05$.

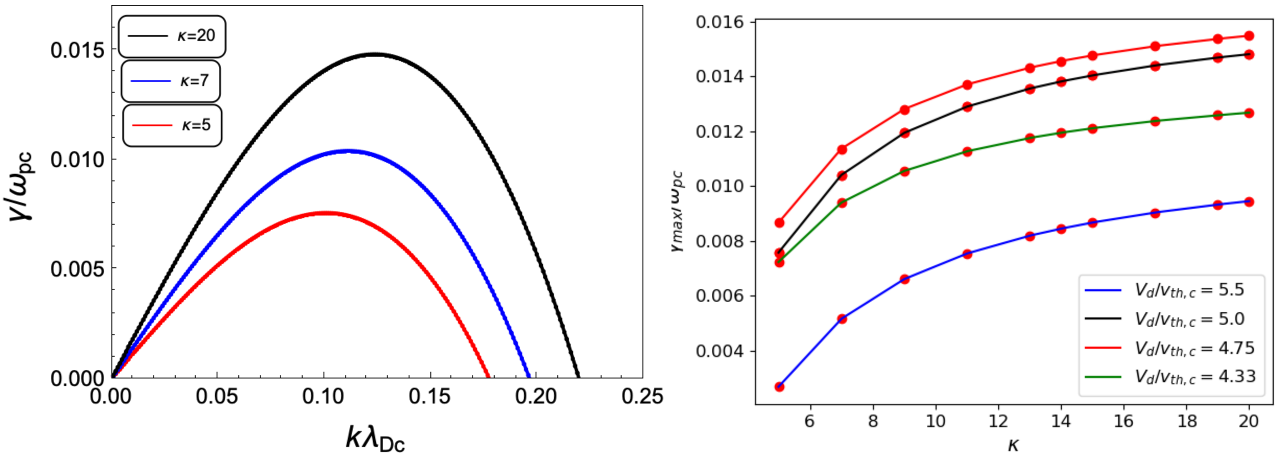

Fig. 2: Dispersion and growth characteristics of the IIAI. Left: Dispersion relation for the IIAI with κ-distributed electrons and $V_d/v_{th,c} = 5$, $n_b/n_c = 0.05$, $T_e/T_c = 10$, and $T_b/T_c = 1$. The black, blue, and red lines are $\kappa = 20, 7$, and 5, respectively. Right: Normalised maximum growth rates, γ_{max}/ω_{pc}, as a function of κ for different proton core-beam drift speeds: $V_d/v_{th,c} = 4.33$ (green line), 4.75 (red line), 5.0 (black line), and 5.5 (blue line). The remaining parameters (n_b/n_c, T_e/T_c, and T_b/T_c) are the same as in panel a.

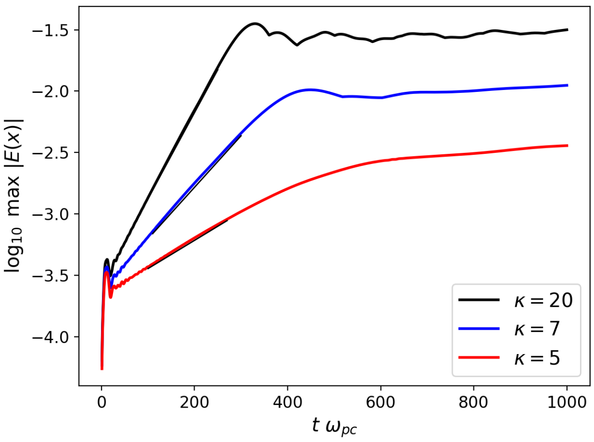

Fig. 3: Temporal evolution of the maximum electric field value for the three simulations with κ-distributed electrons. Derived growth rates (black lines) are $\gamma/\omega_{pc} = 0.0161, 0.0101$, and 0.0053. The simulation parameters are given in Table 1.

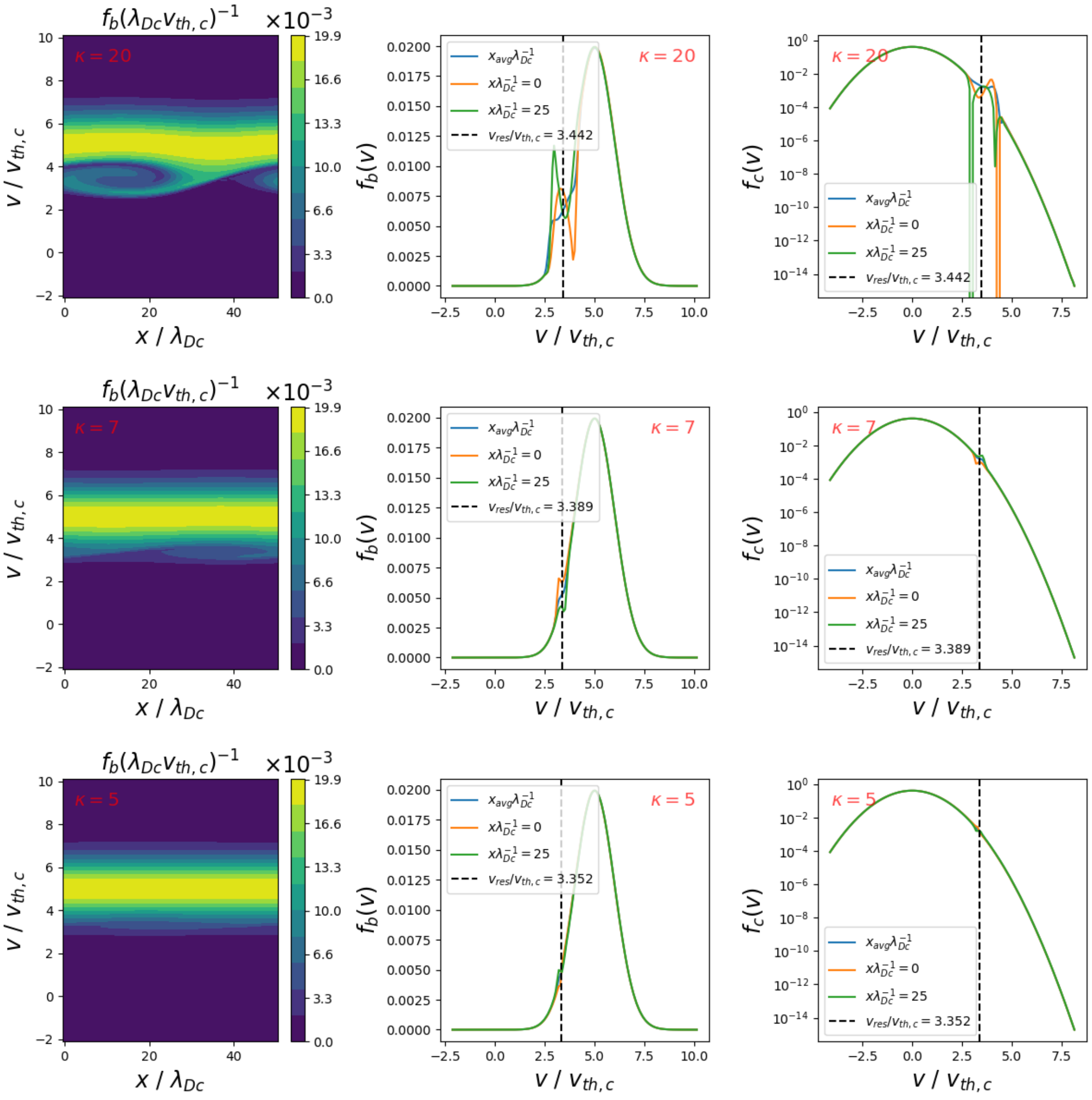

Fig. 4: Snapshots of the proton distributions at time $\omega_{pc}t = 300$, when all simulations are approaching the end of the linear phase, from simulations with electron κ indices $\kappa = 20,\ 7$, and 5. Left: Beam phase-space distribution. Middle and right: Beam and core velocity distributions, respectively, averaged in x (blue lines), cut at $x/\lambda_{Dc} = 0$ (orange line) and at $x/\lambda_{Dc} = 25$ (green line). The vertical dashed lines indicate the theoretical estimates of the resonant velocity.

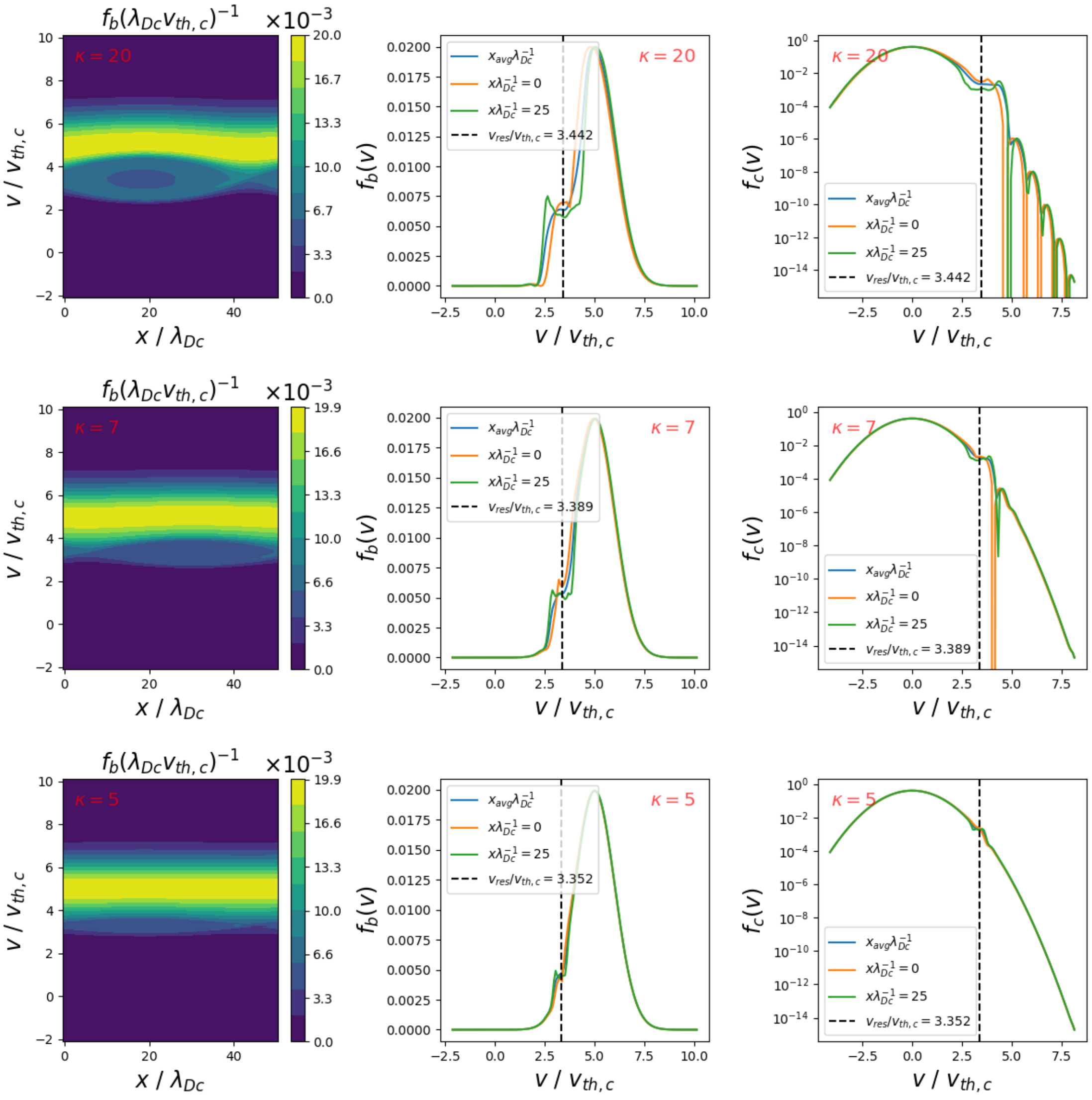

Fig. 5: Same as Fig. 4 but at $\omega_{pc}t = 1000$, when all instabilities have saturated.

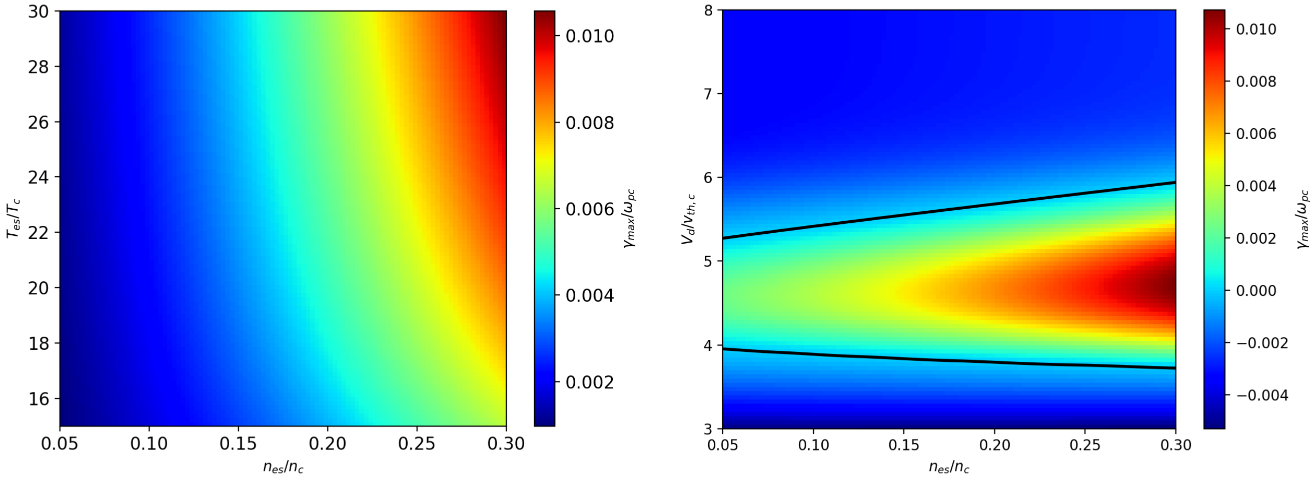

Fig. 6: Maximum growth rate dependence on plasma parameters. Left: Maximum growth rate as a function of n_{es}/n_c and T_{es}/T_c for $V_d/v_{th,c} = 5$, $n_b/n_c = 0.05$, $T_b/T_c = 1$, and $T_{ec}/T_c = 7$. Right: Maximum growth rate as a function of n_{es}/n_c and $V_d/v_{th,c}$ with the same parameters except $T_{es}/T_c = 25$; solid lines indicate the $\gamma = 0$ contour.

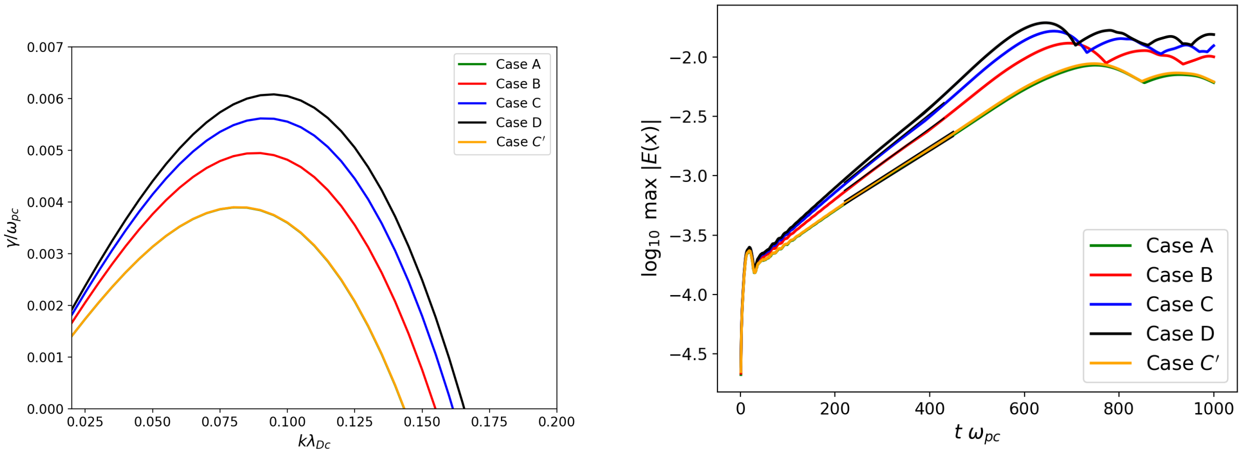

Fig. 7: Dispersion and electric field evolution for the IIAI. Left: Dispersion relation for the IIAI with the parameters given in Table 2. Right: Simulated electric field evolution for the same cases. Common parameters to all cases are $n_b/n_c = 0.05$, $T_b/T_c = 1$, $V_d/v_{th,c} = 5$, and $T_{ec}/T_c = 7$, with electron and proton cores at rest.

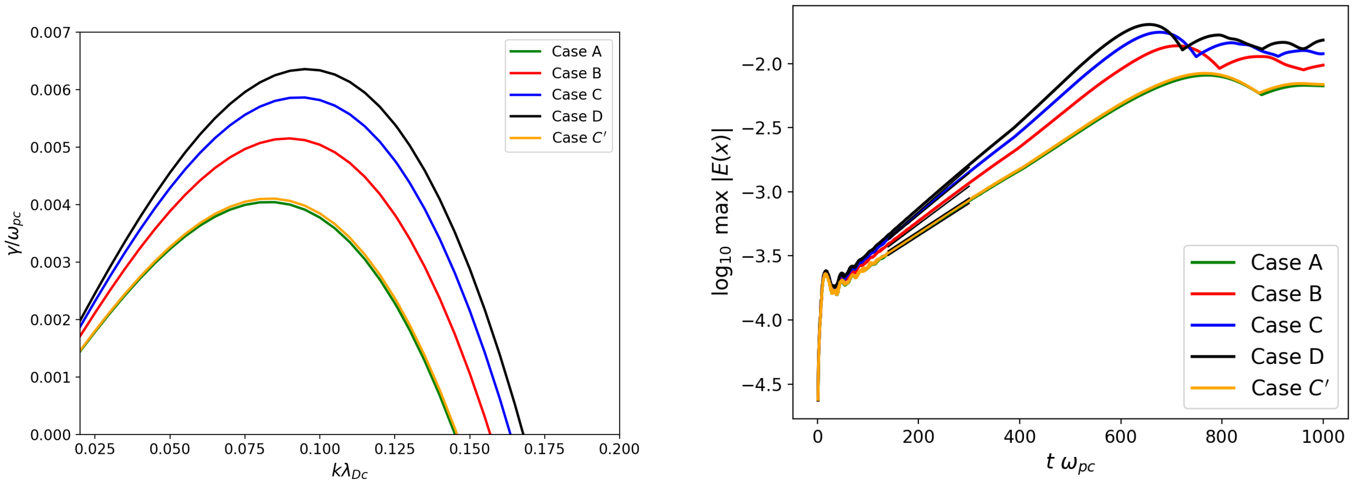

Fig. 8: Same as Fig. 7 but with a single, Maxwellian electron distribution with $T_e = T_{eff}$.

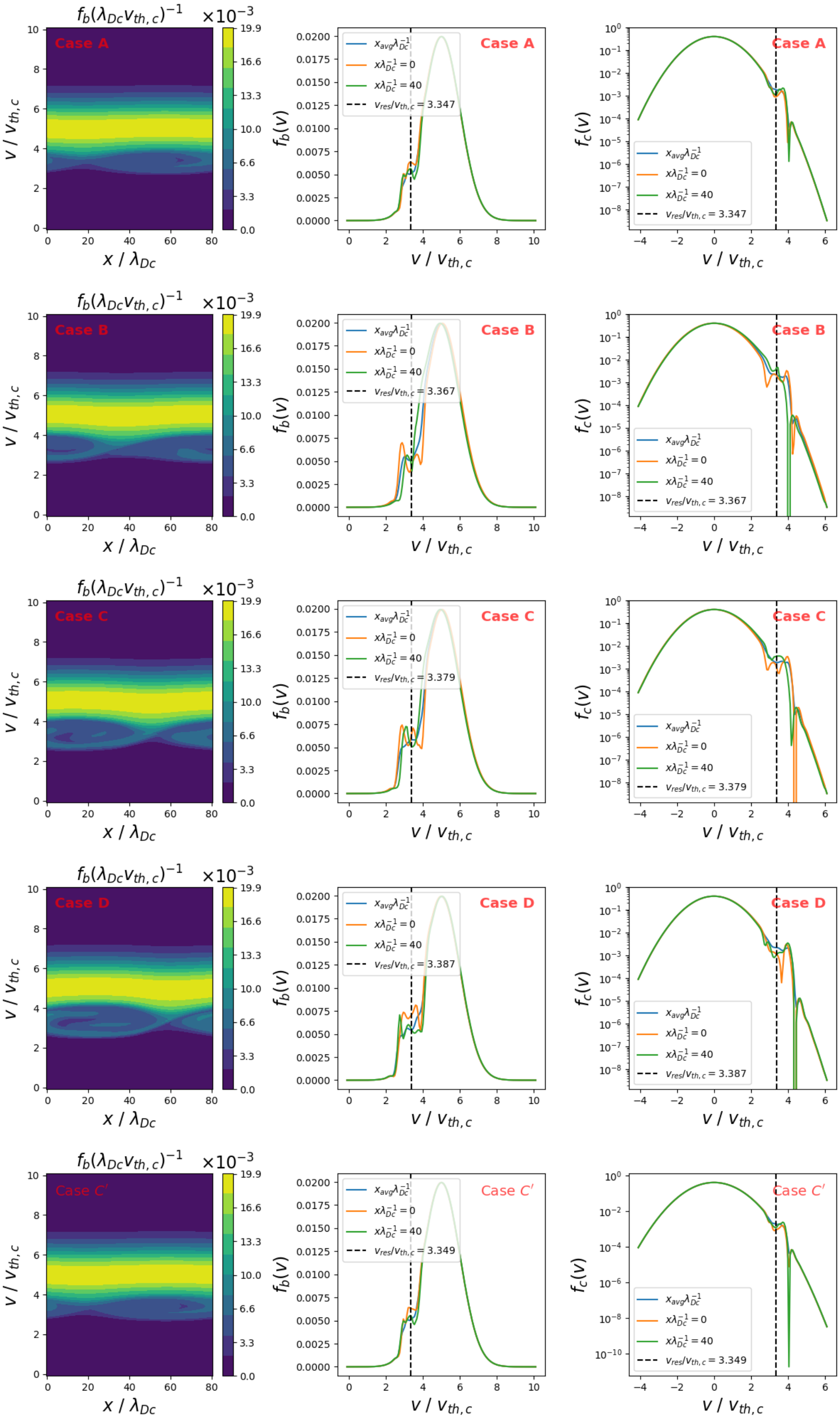

Fig. 9: Snapshots of the core and beam distribution as a function of the strahl's temperature for the cases listed in Table 2 at time $\omega_{pc}t = 1000$, when all simulations are saturated. Left: Beam phase-space distribution. Middle and right: Beam and core velocity distributions, respectively, averaged in x (blue lines), cut at $x/\lambda_{Dc} = 0$ (orange line) and at $x/\lambda_{Dc} = 40$ (green line). The vertical dashed lines indicate the theoretical estimates of the resonant velocity.

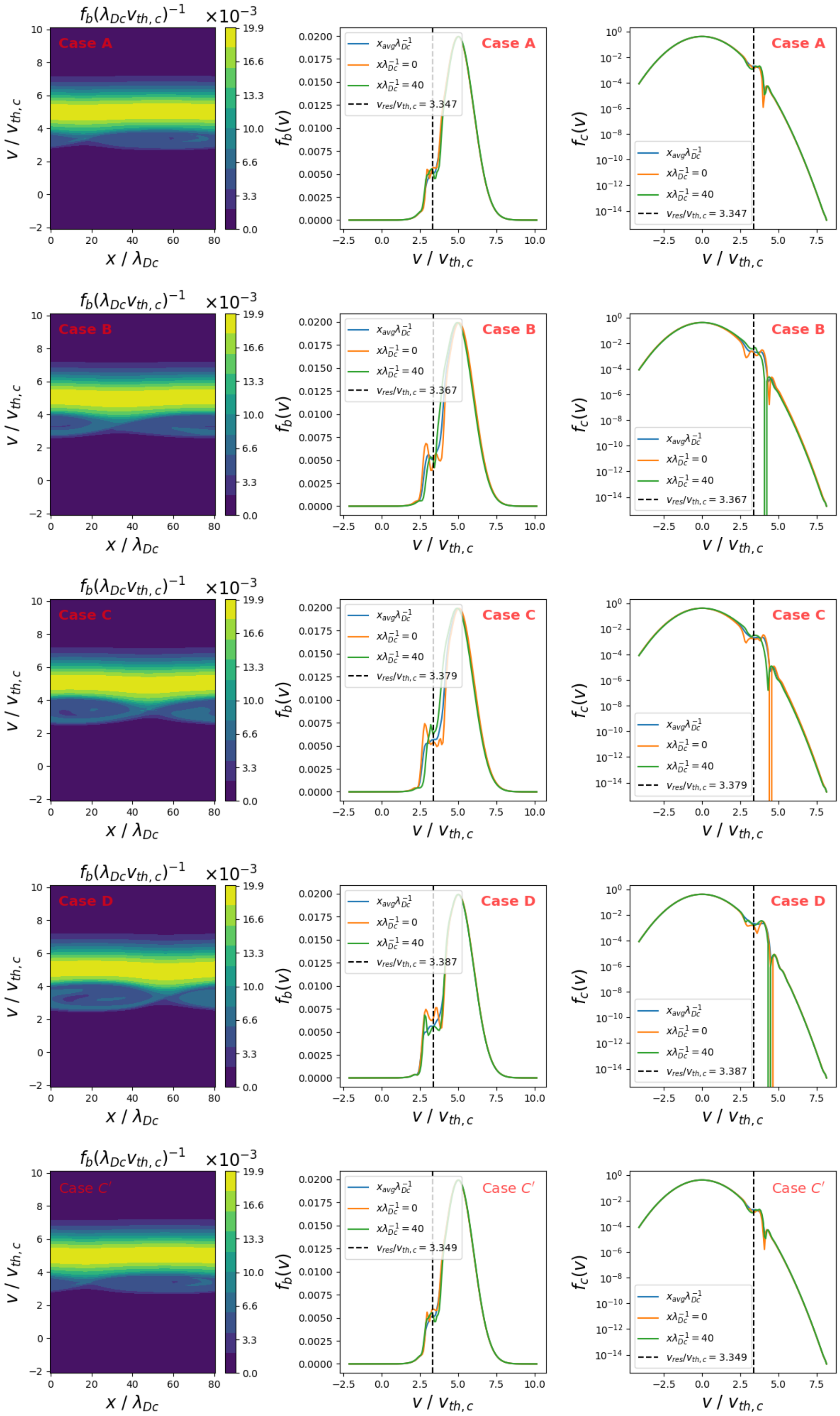

Fig. 10: Same as Fig. 9 but with a single, Maxwellian electron distribution with $T_e = T_{eff}$.

References

Abdul, R. & Mace, R. 2014, Computer Physics Communications

Afify, M. S., Dreher, J., Schoeffler, K., Micera, A., & Innocenti, M. E. 2024, APJ, 971, 93

Ahmadi, N., Germaschewski, K., & Raeder, J. 2016, Journal of Geophysical Research: Space Physics, 121, 5350

Alterman, B., Kasper, J. C., Stevens, M. L., & Koval, A. 2018, APJ, 864, 112.

Bale, S., Kasper, J., Howes, G., et al. 2009, PRL, 103, 211101

Cattell, C., Breneman, A., Dombeck, J., et al. 2021, The Astrophysical journal letters, 911, L29

Che, H., Benz, A. O., & Zank, G. P. 2023, MNRAS, 526, 2110-2117

Daughton, W. & Gary, S. P. 1998, J. Geophys. Res. Space Phys., 103, 20613-20620

Daughton, W., Gary, S. P., & Winske, D. 1999, J. Geophys. Res. Space Phys., 104, 4657-4667

Feldman, W., Asbridge, J., & Bame, S. 1974a, J. Geophys. Res., 79, 2319-2323.

Feldman, W., Asbridge, J., Bame, S., & Montgomery, M. 1973, J. Geophys. Res., 78, 2017–2027.

Feldman, W., Asbridge, J., Bame, S., & Montgomery, M. 1974b, Rev. Geophys., 12, 715-723.

Feldman, W. C., Asbridge, J. R., Bame, S. J., Montgomery, M. D., & Gary, S. P. 1975, JGR, 80, 4181.

Fried, B. D. & Conte, S. D. 1961, The plasma dispersion function: the Hilbert transform of the Gaussian (Elsevier Inc)

Gary, S. P. 1993, Theory of Space Plasma Microinstabilities (New York: Cambridge Univ. Press)

Gary, S. P., Jian, L. K., Broiles, T. W., et al. 2016, J. Geophys. Res. Space Phys., 121, 30-41

Gary, S. P., Madland, C. D., & Tsurutani, B. T. 1985, Phys. Fluids, 28, 3691-3695

Gary, S. P. & Omidi, N. 1987, J. Plasma Physics, 37, 45-61.

Gary, S. P., Smith, C. W., Lee, M. A., Goldstein, M. L., & Forslund, D. W. 1984, Phys. Fluids, 27, 1852-1862

Gary, S. P., Yin, L., Winske, D., & Reisenfeld, D. B. 2000, Geophys. Res. Lett., 27, 1355-1358

Hellinger, P., Travnicek, P., Kasper, J., & Lazarus, A. 2006, J. Geophys. Res. Space Phys., 33, L09101

Jones, W., Lee, A., Gleman, S., & Doucet, H. 1975, Physical Review Letters, 35, 1349

Klein, K., Alterman, B., Stevens, M., Vech, D., & Kasper, J. 2018, PRL, 120, 205102.

Lin, R. 1998, Space Sci. Rev., 86, 61-78.

Lu, Q., Xia, L., & Wang, S. 2006, J. Geophys. Res. Space Phys., 111, A9

Maksimovic, M., Pierrard, V., & Lemaire, J. F. 1997a, A&A, 324, 725-734.

Maksimovic, M., Pierrard, V., & Riley, P. 1997b, Geophys. Res. Lett., 24, 1151-1154

Maksimovic, M., Zouganelis, I., Chaufray, J.-Y., et al. 2005, J. Geophys. Res. Space Phys., 110, A9.

Marsch, E. 2006, Living Rev Sol Phys., 3, 1-100.

Marsch, E. 2018, Ann. Geophys., 36, 1607-1630

Marsch, E., Ao, X.-Z., & Tu, C.-Y. 2004, J. Geophys. Res. Space Phys., 109, A4.

Marsch, E. & Livi, S. 1987, J. Geophys. Res. Space Phys., 92, 7263-7268.

Marsch, E., Mühlhäuser, K.-H., Rosenbauer, H., Schwenn, R., & Denskat, K. 1981, J. Geophys. Res. Space Phys., 86, 9199-9203

Marsch, E., Mühlhäuser, K.-H., Schwenn, R., et al. 1982, J. Geophys. Res. Space Phys., 87, 52-72.

Maruca, B. A., Kasper, J. C., & Gary, S. P. 2012, APJ, 748, 137.

Matteini, L., Hellinger, P., Goldstein, B. E., et al. 2013, JGRA, 118, 2771

Meyer-Vernet, N. 2007, Basics of the solar wind (Cambridge University Press)

Micera, A., Boella, E., Zhukov, A., et al. 2020a, The Astrophysical Journal, 893, 130

Micera, A., Verscharen, D., Coburn, J. T., & Innocenti, M. E. 2025, APJ, 979, 226.

Micera, A., Zhukov, A. N., López, R., et al. 2020b, APJL, 903, L23.

Micera, A., Zhukov, A. N., López, R. A., et al. 2021, ApJ, 919, 42.

Mozer, F., Agapitov, O., Choi, K.-E., & Sydora, R. 2025, APJ 981, 82.

Mozer, F. S., Agapitov, O. V., Kasper, J. C., et al. 2023, AA 673, L3.

Mozer, F. S., Bonnell, J. W., Bowen, T. A., Schumm, G., & Vasko, I. Y. 2020, ApJ, 901, 107

Mozer, F. S., Vasko, I. Y., & Verniero, J. L. 2021, ApJL, 919, L2.

Neugebauer, M., Goldstein, B., Smith, E., & Feldman, W. 1996, J. Geophys. Res. Space Phys., 101, 17047-17055.

Ofman, L., Boardsen, S. A., Jian, L. K., et al. 2023, APJ, 954, 109

Ofman, L., Boardsen, S. A., Jian, L. K., Verniero, J. L., & Larson, D. 2022, APJ, 926, 185

Ofman, L., Boardsen, S. A., Klein, K., et al. 2025, APJ, 986, 119

Pezzini, L., Zhukov, A. N., Bacchini, F., et al. 2024, APJ, 975, 37.

Pierrard, V. & Lazar, M. 2010, Sol. Phys., 267, 153-174.

Pilipp, W., Miggenrieder, H., Montgomery, M., et al. 1987, J. Geophys. Res. Space Phys., 92, 1075-1092.

Reames, D. V. 2021, Solar energetic particles: a modern primer on understanding sources, acceleration and propagation (Springer Nature)

Riquelme, M. A., Quataert, E., & Verscharen, D. 2015, APJ, 800, 27

Silin, V. & Uryupin, S. 1992, Zh. Eksp. Teor. Fiz, 102, 78-89.

Štverák, Š., Maksimovic, M., Trávníček, P. M., et al. 2009, J. Geophys. Res. Space Phys., 114, A5.

Summers, D. & Thorne, R. M. 1991, Phys. Fluids B., 3, 1835-1847

Vasyliunas, V. M. 1968, J. Geophys. Res., 73, 2839-2884

Verniero, J. L., Chandran, B. D. G., Larson, D. E., et al. 2022, ApJ, 924, 112

Verniero, J. L., Larson, D., Bowen, T. A., et al. 2020, ApJS, 248, 5

Verscharen, D., Bourouaine, S., Chandran, B. D. G., & Maruca, B. A. 2013, APJ, 773, 8

Verscharen, D. & Chandran, B. D. 2013, APJ, 764, 88

Verscharen, D., Klein, K. G., & Maruca, B. A. 2019, LRSP, 16, 5

Verscharen, D. & Marsch, E. 2011, Ann. Geophys., 29, 909-917

Virtanen, P., Gommers, R., Oliphant, T. E., et al. 2020, Nat. Methods., 17, 261–272

Walters, J., Klein, K. G., Lichko, E., Juno, J., & TenBarge, J. M. 2024, APJ, 975, 290.

Wang, X. & Lin, Y. 2003, Phys.Plasmas, 10, 3528-3538

Yoon, P. H., López, R. A., Salem, C. S., Bonnell, J. W., & Kim, S. 2024, Entropy, 26, 310

Ďurovcová, T., Šafránková, J., & Němeček, Z. 2019, SoPh, 294, 97